

Instrumented Pyramid Adapter for Amputee Gait Analysis and Powered Prosthesis Control

Lukas Gabert^{ID} and Tommaso Lenzi^{ID}, *Member, IEEE*

Abstract—Novel advanced prostheses aim to improve the ambulation ability of lower-limb amputees by adapting the prosthesis mechanical behavior online during ambulation. Accurate force/torque sensing is necessary to measure the physical interaction between the user, the prosthesis, and the environment. Most available solutions consist of retrofitting an off-the-shelf load cell, which leads to suboptimal designs regarding weight and size, ultimately reducing the prosthesis usability. To address this limitation, we propose to instrument an existing prosthesis component, namely, a pyramid adapter, with force/torque sensing and an inertial measurement unit. Magnetic sensing of large structural deformations is used to improve system reliability and reduce costs. Testing shows that the proposed sensor prototype can sense up to 120 Nm and 2500 N of torque and force and has 2.1% and 8.3% nonlinearity, respectively, during walking. The total weight is 150 g—only 66 g more than a standard pyramid adapter without force/torque instrumentation. Amputee testing with robotic leg prosthesis is conducted to validate the instrumented pyramid in a case scenario.

Index Terms—Ambulation, force/torque sensing, prosthetics.

I. INTRODUCTION

LOWER-LIMB amputation affects over 600,000 people in the United States alone and is becoming more common, primarily due to the increased incidence of peripheral vascular disease [1]. The loss of a lower limb can adversely impact ambulation ability and quality of life [2]. Ambulation with available lower-limb prostheses is slow, inefficient, and unstable [3]–[5]. As a result, individuals with lower-limb amputations walk on average 3000 steps per day compared to an average of 5100 steps per day for non-amputees [6], [7]. Novel prosthesis technologies have recently been developed to address these challenges [8]. These new technologies aim to improve ambulation by adapting the prosthesis mechanical behavior based on the user's needs. For example, semi-active microprocessor-controlled prostheses change the damping and stiffness of the prosthetic joint during locomotion as a function of ground force. Similarly, more advanced powered prostheses provide positive power to propel gait in stance and actively generate the swing movement [9]. Thus, these novel prosthesis technologies require accurate force/torque sensing to measure

the physical interaction between the user, the prosthesis, and the environment.

The development of force/torque sensors for prosthetic applications requires satisfying competing design requirements in terms of a wide force and torque range and a small, lightweight package. During common ambulation activities, torque and force at the ankle, normalized by the user's body weight, peak at about 1.7 Nm/kg and 11.4 N/kg [10], respectively. This relatively wide range of torque and force is easier to satisfy if the sensor dimensions and weight are not critical. However, in prosthetic applications, the size of the force/torque sensor affects the overall prosthesis dimensions, especially the build height, which ultimately determines how many people can use the prosthesis [11]. Moreover, increasing the prosthesis weight affects gait negatively by increasing metabolic consumption and muscle effort [12], [13]. As a result, it is important to minimize build height and weight in sensors used for prosthetic applications.

Many different methods are used to sense force and torque in available prosthetic devices. A common force/torque sensing solution consists of using an off-the-shelf load cell in line with the prosthesis [14], [15]. This design solution is not optimal due to the additional weight and size of the mechanical components used to interface the sensor with the prosthesis. To reduce the added mass, some researchers use sensors with lower than necessary torque range at the cost of force/torque saturation. An alternative approach is to develop a custom force/torque load cell. This approach leads to a lower overall prosthesis weight and build height as a result of a better sensor integration with the prosthesis design [16]–[18] but is rather complex to achieve. Others have opted to reduce complexity and weight by giving up on combined force/torque sensing and using uniaxial force [19], uniaxial moment [20], or simpler contact sensing [21]. Pressure sensing, using force sensing resistors under the prosthesis foot [22], [23], or within components [24], [25], has also been used as an alternative solution to direct load cells. Hall effect sensing for multiaxial load cells has also been proposed [26], although the current force/torque range is unsuitable for prosthetic applications. Finally, some devices have been developed without force/moment sensing, using inertial measurement units to detect the contact of the foot with the ground [27], [28]. The development of a lightweight, robust, and effective force torque sensor for prosthetics applications remains an open challenge.

In this paper, we present a compact and lightweight force/torque sensor for prosthetic applications based on contactless magnetic-field sensing, shown in Fig. 1 (c). As we

Manuscript received April 12, 2019; accepted May 15, 2019. Date of publication May 31, 2019; date of current version August 15, 2019. This work was supported in part by the U.S. Department of Defense under Grant W81XWH-16-1-0701. The associate editor coordinating the review of this paper and approving it for publication was Prof. Vedran Bilas. (*Corresponding author: Lukas Gabert.*)

The authors are with the Department of Mechanical Engineering, Utah Robotics Center, University of Utah, Salt Lake City, UT 84112 USA (e-mail: lukas.r.gabert@utah.edu; t.lenzi@utah.edu).

Digital Object Identifier 10.1109/JSEN.2019.2920179

1558-1748 © 2019 IEEE. Personal use is permitted, but republication/redistribution requires IEEE permission.
See http://www.ieee.org/publications_standards/publications/rights/index.html for more information.

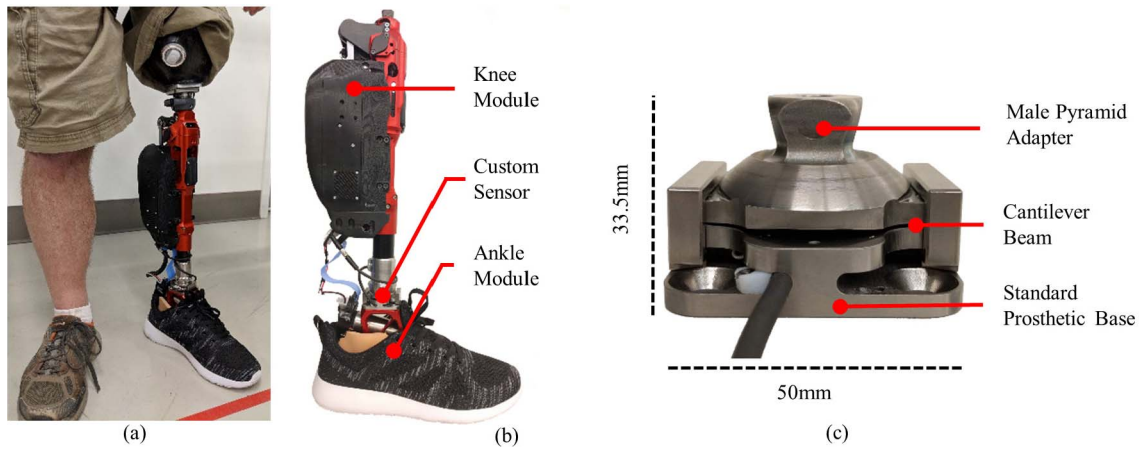


Fig. 1. (a) The Utah Lightweight Leg and sensor on a subject with an amputation. (b) Side View of the Utah Lightweight Leg with the prototype sensor. (c) Close-up view of the fabricated sensor with dimensions.

will show, a symmetrical cantilever beam design can achieve higher deformations than common force/torque sensors based on strain gauges, thus enabling contactless magnetic-field sensing. Additionally, we will show that the force/torque sensing elements in the proposed design can be easily integrated into a male pyramid adapter, which is commonly used in prosthetics, minimizing the overall weight and build height of the proposed force/torque sensor. The design requirements are obtained from available biomechanics datasets, as shown in Section II.A, and used to drive the sensor design. Analytical and numerical models (II.B, II.D) are developed to guide the structural design. Finally, the sensing elements and conditioning electronics are integrated into the system to maximize sensitivity for the desired force and torque range and robustness. The sensor is calibrated through extensive bench top testing and validated on a passive prosthesis with an able-bodied user and a powered prosthesis with an amputee user.

II. DESIGN AND DEVELOPMENT

A. Design Requirements

The design of a force/torque sensor largely depends on the tradeoff between the number of sensitive axes and their full-scale values, as well as the size, weight, and sensitivity of the sensor. To minimize weight and size, our design focuses on axial forces along the shank and sagittal-plane moments only. Based on available biomechanics datasets, a 70-kg person walking on level ground produces a maximum torque of 120 Nm at the ankle and 50 Nm at the knee in the sagittal plane and 800 N along the shank [10]. Moreover, during stairs ambulation, the maximum torques at the joints are 120 Nm in the ankle and 100 Nm at the knee [10]. In addition, the forces and torques measured on prosthetic joints are typically lower than those seen on able-bodied joints [29]. Thus, we use the maximum torque and force obtained from available able-bodied datasets to drive the design of the proposed sensor. Also, to satisfy powered prosthesis requirements, the sensor needs to be accurate enough to be used for prosthesis control as well as gait analysis tasks. Specifically, we want to use

TABLE I
DESIGN REQUIREMENTS

Requirement	Value
Axial Force	≥ 800 N
Sagittal Torque	≥ 120 Nm
Length/Width	50x50 mm
Height	22 mm
Weight	81 g
Error in Gait	$\leq 3\%$ Full-Scale
Resolution	≤ 20 N

the sensor to accurately and timely detect the contact with the ground, as well as to measure ground reaction force and torque for gait analysis. To achieve this goal, we want a root mean squared error of 3% of full-scale or better, as this would be in line with current commercially available gait analysis devices such as the iPecsTM(Intelligent Prosthetic Endo Component System; College Park Industries, Michigan, USA) [30]. A sensitivity of 5% of full-scale is also needed for the sensor, as 5% of body weight is a common threshold to identify toe-off and heel-strike events during walking [31]. The sensor requirements are summarized in TABLE I.

The proposed sensor is designed to interface with off-the-shelf prosthetic components so that it can be used in most available prostheses without significantly affecting their design and how they are fit to users. To this end, we modeled the sensor design off of a 4-hole male pyramid adapter (Fig. 2(a)), which is commonly used to connect prosthesis modules, such as the socket, the knee module, and the ankle/foot module. With this design, the prosthetist does not need to add extra components and can instead replace an existing component of the prosthesis with this sensor. To be interchangeable with off-the-shelf 4-hole male pyramid adapters, the sensor must have (1) a length and width which do not exceed a common size of 50 mm, (2) a standard male pyramid on one side, and (3) a 36 mm square clearance hole pattern on the other side. Ideally, the height must not exceed that of a common 4-hole pyramid, such as 22 mm for the Bulldog 4-hole stainless steel adapter (Model P3-WH, Bulldog Tools, Inc., Ohio, USA).

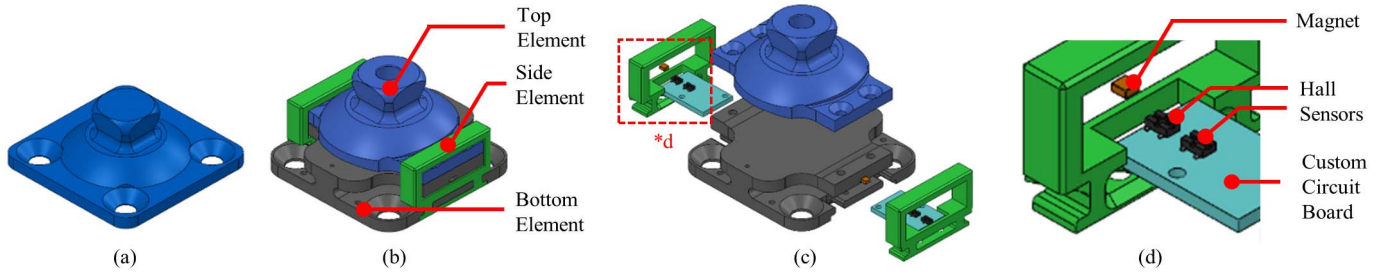


Fig. 2. (a) A standard male pyramid adapter. (b) – (d) Isometric, exploded, and close-up views of the proposed sensor, respectively.

However, height is not a stringent requirement as prosthetic components are commonly attached to tubing, which can be shortened if the height of another component is lengthened. The physical dimensions and hole pattern of common male pyramid adapters provide clear design requirements for our custom sensor to interface with existing prosthesis designs, thus increasing the number of use cases and ease of use of the device, while providing additional sensing function without needing extra space.

The sensor is also designed to match the weight of off-the-shelf prosthetic components. Increasing prosthetic mass can harm gait symmetry and increase metabolic costs [12], [13]. Additionally, a proximal center of mass creates a more efficient gait [32], so the weight of any component which may be attached distally should be reduced. As an example of the weight of prosthetic components, the previously mentioned Bulldog adapter model P3-WH weighs 84 g. Currently available devices for measuring force and torque can weigh significantly more than this, such as the iPecs™, which weighs 280 g. The iPecs™ sensor, in addition to its weight, needs additional hardware to attach to the prosthesis, which adds to the mass. However, it has the capabilities to measure force and torque in all three axes. Commercially available 6-axis load cells, such as the JR3 model 45E15A4 (JR3 Inc., California, USA) have more accurate force and torque sensing (1000/2000 N and 125 Nm), but weigh significantly more (1150 g without the conditioning electronics and the mechanical interfaces required to interface the load cell with the prosthesis). State-of-the-art microprocessor-controlled knee prostheses, such as the Ottobock C-Leg, use an instrumented pylon to achieve force sensing [33]. Although the weight of the force/torque sensor embedded in the pylon is not disclosed, it can be obtained by comparing the instrumented pylon with its conventional counterpart. An uncut C-Leg pylon weighs 280 g, whereas a conventional pylon with the same diameter and length weighs 240 g. Thus, we can conclude that force/torque sensing in the C-Leg adds 40g to the prosthesis design, although we do not know the performance of the sensor. Ideally, a force/torque sensor should have similar weight to the prosthetic component it is meant to replace to minimize negative impacts on the gait of the user. However, this may not be possible due to the addition of necessary components for force/torque sensing.

B. Design Implementation

Fig. 2 compares the design of an off-the-shelf male pyramid adapter (a) with our custom sensor (b), including an exploded

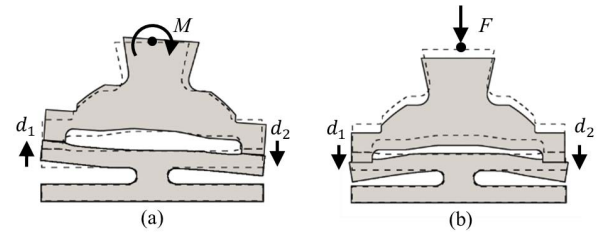


Fig. 3. Exaggerated deformation based on (a) Torque; (b) Vertical force.

view with highlights to the main sensor components (c, d). As shown by the CAD model in Fig. 2 (b-d), the sensor comprises three main structural elements and two sensing elements. The top element (shown in blue in Fig. 2(b-c)) features a standard male pyramid shape to connect with off-the-shelf prosthetic components. Its primary function is to safely transfer the force and torque applied by the user to the bottom element, which comprises the sensing elements, while hosting the inertial measurement unit board. The bottom element (shown in grey in Fig. 2(b-c)) connects with the top element through two deformable structures similar to cantilever beams and connects with the prosthesis frame using a standard four-hole configuration. In addition, the bottom element houses two magnets (shown in orange in Fig. 2(c-d)), located in the two ends of the cantilever beams to obtain force/torque transduction. Hall sensors (black in Fig. 2(c-d)), positioned on custom circuit boards (light blue in Fig. 2(c-d)), are placed beneath the magnets and fastened to the fixed part of the bottom element. Two identical side elements (green in Fig. 2(b-d)) are added to the sensor structure to work as mechanical end-stops limiting the deformation of the bottom element within safe margins of deformation.

The three mechanical elements and two sensing elements concurrently determine the function of the sensor using a two-stage transduction principle. As can be seen in Fig. 3, the torque and force applied on the top element through the male pyramid adapter are transferred to the bottom element, causing an elastic deformation of its mechanical structure. In turn, the elastic deformation of the mechanical structure creates a millimeter-scale displacement at the two mobile ends of the bottom element, which are indicated using d_1 and d_2 . For example, a pure moment applied to the top element causes the two ends to move in the opposite direction (Fig. 3 (a)), whereas a pure force applied to the top element causes the two ends of the bottom element to move in the same direction (Fig. 3 (b)). This displacement causes the two

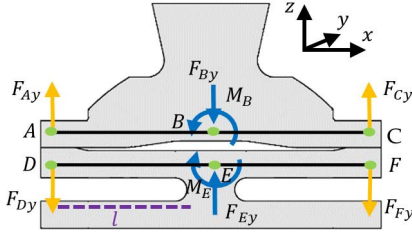


Fig. 4. Analytical diagram of sensor design. Applied forces and moments in blue and reaction forces in yellow.

magnets embedded in the mobile ends of the bottom element to move relative to the Hall sensors, which are located on the fixed part of the bottom element. As the magnetic field sensed by the Hall sensors changes as a function of the magnet position, the elastic deformation of the bottom element due to the force and torque applied to the top element is transduced into voltage. Thus, the first transduction step translates a force into a displacement while the second transduction step translates a displacement into a change of magnetic field strength which is sensed by the Hall sensors. Both steps of the transduction principle significantly affect its ability to measure force and torque and were co-designed to satisfy the design requirements.

The structural elements of the sensor were designed to translate a micrometric elastic deformation of the mechanical structure into a millimetric displacement of the magnets located on the two mobile ends of the bottom element. Fig. 4 shows a side view of the sensor CAD model with a free-body diagram of its mechanical structure. Line segments ABC and DEF are separated for analytical purposes. Structurally, points A and D are connected, and points C and F are connected, which means that the forces within each set of points are equal and opposite. The load is applied to the pyramid adapter at point B, and a reaction load is created at point E, where the structure is fixed to ground or a prosthetic device through the 4-hole pattern. In the structure, point E is rigidly constrained, as it is connected to the 4-hole pattern on the bottom of the sensor with a profile which has negligible deflection under the loads expected for this sensor. Due to this constraint on point E, we can treat line segments DE and EF as cantilever beams.

The profile of the cantilever beams affects the function of the sensor by determining the displacement of the magnets for a given torque and force applied to the sensor. The dimensional requirements outlined in II.A provide an upper bound for the design of the beam. The measurable displacement of the magnets depends on the curvature of the beam ρ , which, in turn, introduces a stress σ . The stress in the beam heavily affects the life cycle and structural integrity of the sensor. Thus, curvature must be minimized in the design of the sensor. Equation (1) outlines the relationship between curvature, stress, modulus of elasticity, E , and height of the beam, y . For a given displacement of the beam ends, the stress is largest for a point farthest from the neutral axis, so to minimize stress, we want to decrease the distance y , which is half the beam thickness, T . Another way to decrease stress

is to increase the radius of curvature of the beam, which means that we should maximize the length of the beam, l . Equation (2) shows that to decrease stress, we want to increase the second moment of inertia, I . To do this while keeping T to a minimum means that we should increase the depth, D , to the maximum boundary allowed by the dimensions in II.A. The modulus of elasticity should be low enough that the material does not break before it bends, but high enough that the material has enough rigidity within the dimensions outlined. To satisfy these requirements, we chose Titanium Grade 5. In addition, Titanium Grade 5 is a non-ferrous material, which is required by the proposed magnetic transduction principle (II.C). Through this analysis, we see that all dimensions should be maximized within confines provided by section II.A except for thickness, which needs to be specifically optimized for the loading and sensitivity needed.

$$\sigma = -\frac{E y}{\rho} \quad (1)$$

$$\sigma = -\frac{M y}{I} \quad (2)$$

To determine the necessary thickness of the beam profile, we need to analyze the forces on the beams. The forces on the ends of the beams can be written as shown in (3).

$$F_{Dy} = \frac{M_B}{2l} + \frac{F_{Bz}}{2} \text{ and } F_{Fy} = \frac{-M_B}{2l} + \frac{F_{Bz}}{2} \quad (3)$$

With force applied at the free end in the vertical direction, the equations for displacement of a cantilever beam are shown in (4) [34].

$$y_A = -\frac{F_{Dz} l^3}{3EI} \text{ and } \Theta_A = \frac{F_{Dz} l^2}{2EI} \text{ where } I = \frac{DT^3}{12} \quad (4)$$

In this design, the two cantilever beams, represented by line segments DE and EF, are attached with screws to the pyramid adapter at the top, represented by line segment ABC. The attachment constrains the rotational displacement at the ends of the beams to be equal and opposite, assuming ABC is rigid enough that any deformation is negligible. The displacement of a guided cantilever beam, in which the rotation of the ends is constrained to zero [34], is shown in (5).

$$y_A = -\frac{F_{Dz} l^3}{12EI} \text{ and } \Theta_A = 0 \quad (5)$$

Combining (3), (4), and (5), we get a displacement of point A for both a free and guided beam as shown in (6) and (7), respectively.

$$y_{A,free} = \frac{-4 \left(\frac{F_{Bz}}{2} + \frac{M_B}{2l} \right) l^3}{EDT^3} \quad (6)$$

$$y_{A,guided} = \frac{- \left(\frac{F_{Bz}}{2} + \frac{M_B}{2l} \right) l^3}{EDT^3} \quad (7)$$

The analytical model shows that the critical design parameters that define the mechanical transduction are length (l), thickness (T), depth (D), and Young's Modulus (E) of the cantilever beams. The pyramid connector does not constrain the ends of the beams to be at zero rotation in all cases, but it does not allow for free rotation. This limit of rotation

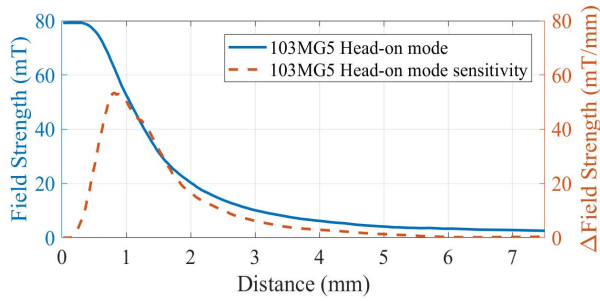


Fig. 5. Honeywell 103MG5 magnetic field strength and sensitivity.

creates a scenario in which the cantilever beams do not behave in accordance with either (6) or (7), but instead behave somewhere in the space between the two equations. Solving equations 6 and 7 using the parameters $E = 114$ GPa, $y = 5$ mm, $D = 24$ mm, $F = 1000$ N, $M = 120$ Nm, and $l = 20$ mm, we see that the cantilever beams should be somewhere between 1.3 and 5.1 mm in thickness. This well-defined range of thicknesses can be modeled parametrically using Abaqus (Dassault Systèmes, Paris, France) to determine a beam thickness that satisfies all design requirements.

C. Electrical/Magnetic Transduction

The physical displacement between the ends of the cantilever beams and the bottom element is translated into an electrical signal using Hall effect sensing, which accomplishes the force/torque transduction. Hall effect sensing introduces a further nonlinearity in the sensor transduction principle. Fig. 5 shows the non-linear field strength of the Honeywell 103mg5 magnet (Honeywell International Inc, North Carolina, USA), which fits into the proposed sensor structure [35]. From Fig. 5, we can see that the sensitivity of the Hall sensor, which is shown by the orange dashed line, is lower than 20 mT/mm when the distance between the Hall sensor and the magnet is smaller than 0.5 mm. Similarly, the Hall sensor has low sensitivity when the distance from the magnet is greater than 2.5 mm. This analysis of the magnetic field strength and sensitivity curve determines the ideal displacement of the beam ends and is considered in the structural design of the sensor.

A custom board was developed to host the electronic components necessary for the proposed force/torque transduction. The schematic diagram of the custom board is shown in Fig. 6 (a), while Fig. 6 (b) shows a fabricated board. Two identical circuit boards were built and located under each cantilever beam as shown in Fig. 7 (a). Each board includes two 1-dimensional Hall sensors (A1308, Allegro Microsystems, New Hampshire, USA). The primary Hall sensor is placed directly under the magnet, and a reference sensor is placed farther inside the sensor body by 9 mm, as shown in Fig. 7 (b). This internal Hall sensor is used to compensate for stray magnetic fields, which are commonly seen in powered prostheses due to the presence of electromechanical actuators. Because the magnetic field generated by the permanent magnet (Red element in Fig. 7) is negligible for a distance greater than 6 mm (blue line in Fig. 5), placing the reference sensor

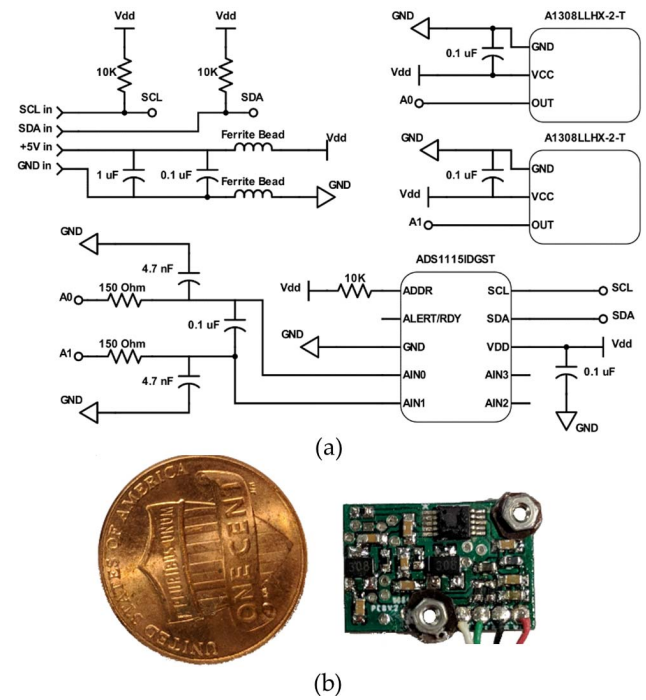


Fig. 6. Custom electronics. (a) The electrical circuit diagram. The pullup resistor from ADDR on the ADC can be switched to pulldown to change the address of the device on the I2C bus. (b) A fabricated board with a penny for reference.

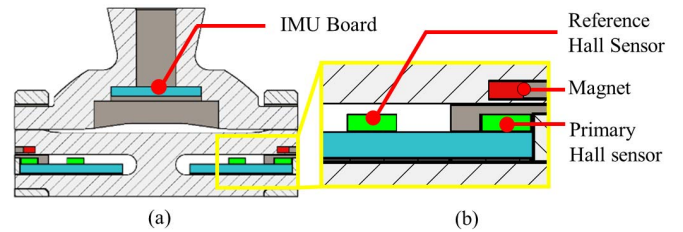


Fig. 7. (a) Section view of the device showing electrical component placement. (b) Close-up view of the Hall sensor and magnet placement.

9 mm away shields it from the effects of the magnet. At the same time, 9 mm is close enough to the primary sensor that the reference sensor will create a similar voltage output due to a stray magnetic field. The stray field is compensated by attaching the outputs of both Hall sensors to a differential input.

The Hall sensors are wired to the differential input of a 16-bit analog-to-digital converter (ADS1115, Texas Instruments, Texas, USA). The ADS1115 has a small footprint (5×3 mm) and can sample a single differential input at up to 860 Hz while applying digital filters and transmitting the filtered input using I²C. Outputs of the Hall sensors are filtered using a low-pass first order resistor-capacitor (RC) filter with two common mode filter capacitors. This analog filter limits the effects of aliasing and reduces external noise. In addition, the differential ADC input rejects common-mode noise, which increases the performance of the sensor. The magnetic field range, as shown in Fig. 5, ranges from about 26 to 68 mT for a distance between the magnet and sensor

of 1.2mm, assuming a deformation of 0.5mm. Shims can be placed under the circuit board in order to meet this distance requirement, even with manufacturing error. The ADS1115 has a resolution of 62.5 μ V per least significant bit, and the Allegro A1308 outputs 25 mV/mT. Thus, the sensor has a resolution of 16,800 discrete points over the proposed range. The custom boards are connected with an off-the-shelf breakout board of the inertial measurement unit (IMU) MPU9250 (TDK Corporation, Tokyo, Japan), which is a 16-bit 9-axis accelerometer, gyroscope, and magnetometer. The IMU placement within the sensor is shown in Fig. 7 (a). The custom circuit boards and the IMU breakout board communicate on the same I2C bus, [so the sensor requires only one I2C connection. The sensor is capable of greater than 500 Hz operation on I2C fast mode while outputting gyroscope and acceleration data in 3 dimensions, as well as both Hall sensor voltages.

D. Simulations and Dimensioning

The analytical model described in II.B provided a range of beam thicknesses which would create the required deformation under expected loading. Starting from this range, Abaqus was used to determine the final thickness of the beams. Specifically, simulations were performed using Abaqus to analyze the structure shown in Fig. 8 with the material set as Titanium Grade V. From II.C, we know that we want a range of $1.2 \text{ mm} \pm 0.5 \text{ mm}$, as that will keep us in the high sensitivity area of the magnetic curve. To obtain a more accurate result, we analyzed the displacement of the ends of the beams using the force and torque combinations that would be generated by a 70 kg person walking on level ground if the sensor were located at the ankle) [36]. Notably, the ankle sees higher torques than the knee during ambulation) [36]. A plot of the force and torque used for simulation is shown in Fig. 9 (a). By using biological force and torque data we can determine if there are any loading conditions which create undesired displacement during the gait cycle, such as a displacement which is too small during stance, or too large during push-off. The force and torque are applied at point A, and the displacement is measured at points B and C. We analyzed beam thicknesses between 1.5 and 4.5 mm, as that covers most of the range indicated in II.C. The result of the analysis is shown in Fig. 9 (b), in which the maximum value of displacement for either point B or C is shown, depending on which is larger. For a beam thickness of 3.66 mm, shown by the red line in Fig. 9 (b), the analysis shows a displacement of 0.517 mm, which is close to the desired maximum displacement of 0.5 mm. Therefore, we use 3.66 mm as the starting thickness of the structure which we model and analyze in II.E.

E. ANSYS Analysis

Using a starting thickness of 3.66 mm, the form of the sensor was refined to lower stress concentrations and comply with size requirements. We used Ansys (Ansys Inc., Pennsylvania, USA) to determine the displacement and integrity of the structure under loading. The structure was modeled as Titanium Grade V. A sample analysis for 120 Nm of pure torque is shown in Fig. 10 (a), and an analysis of 2500 N of

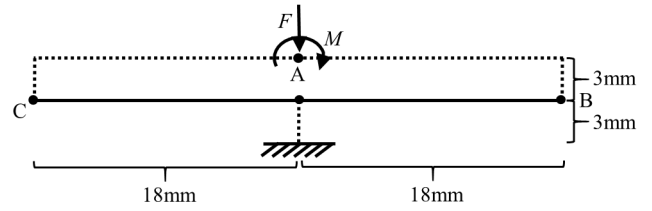
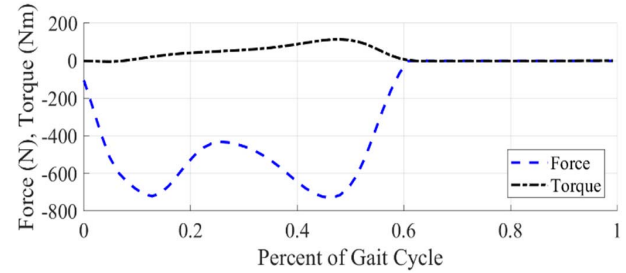
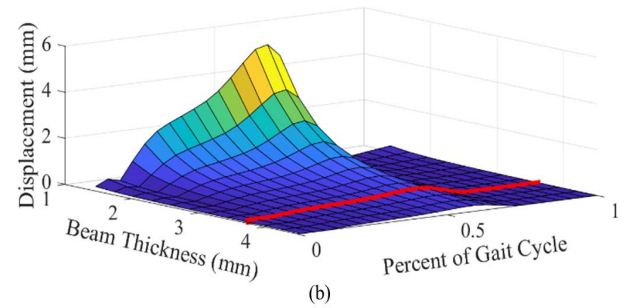


Fig. 8. Diagram of the geometry in Abaqus. The dashed lines are modeled with a cross-section of 23x5 mm, and the solid lines are modeled with a depth of 23 mm and a parametrically varied height. F and M are parametrically varied, and the displacement of points B and C are recorded.



(a)



(b)

Fig. 9. (a) Biological data used to simulate loading during walking. (b) Displacement of beams of different thicknesses throughout the gait cycle. The red line highlights the thickness of 3.66 mm used for ANSYS calculations.

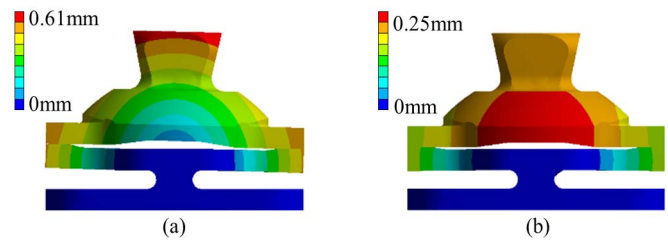


Fig. 10. FEA displacement results for (a) 120 Nm of torque. (b) 2500 N of vertical force. The displacement of the ends of the beams is 0.48 mm and 0.17 mm for torque and force, respectively.

pure force is shown in Fig. 10 (b). All analyses were checked for convergence. The analysis shows a stiffness of 6.2 kNm/rad in pure torque and 15 MN/m in pure force, with a safety factor of 1.7 and 3.8, respectively.

III. EXPERIMENTAL VALIDATION

A. Calibration

The device was calibrated to obtain accurate force and torque readings using an Instron 4303 (Instron, Massachusetts, USA). The calibration was conducted in compression using

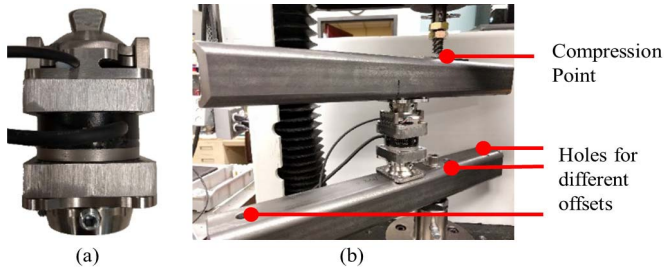


Fig. 11. (a) The sensor attached to the top of an SRI M3713D 6-axis load cell. (b) A photo of the testing setup, showing the ability to change the sensor offset from the compression point in order to create different force/torque ratios.

TABLE II
COMPRESSION TESTING PARAMETERS

Force (N)	Offset (mm)	Speed (mm/min)
2500	0	0.5
2500	23.5	1
2000	52	2
1500	77.5	4
650	177.5	8
310	377.5	16

a 6-axis load cell (SRI-M3713D, Sunrise Instruments) as a reference for the forces and torques. As shown in Fig. 11 (a), the reference load cell was placed in line with our custom sensor. Moreover, the sensors were located at an offset from the point of compression for some tests in order to create a torque, as shown in Fig. 11 (b). To account for the vertical offset between the reference load cell and our custom sensor in the testing setup, we subtract the contribution of the horizontal force measured by the reference sensor from the moment measured by the custom sensor using (8), where m_x is sagittal torque, f_y is horizontal force, and D is the vertical offset between the two sensors.

$$m_{x,corrected} = m_x - f_y D \quad (8)$$

The compression testing parameters used for calibration are shown in TABLE II. Each compression test was repeated three times. Compression tests which included an offset were repeated with the sensor flipped in order to characterize both positive and negative torques. As such, we performed a total of 33 compressions for calibration.

The tests were performed at a rate, shown in the third column of TABLE II, which equates to quasi-static loading. The time to full load was approximately 100 s for each test. For offset tests which create torque, the speed of the machine was increased proportionally to distance. This is because for the same rotational deformation of the sensor, the compression head must move a greater distance when it is farther away.

In order to verify the performance of the calibration under different loading speeds, we conducted additional compression tests at an offset of 23.5 mm and a loading value of 1500 N. We compared the force and torque measured by the proposed sensor, calculated using the fitting from III.B, with the output of the SRI sensor. The results are shown in TABLE III. The tests found the root-mean-squared-error (RMSE) changes by

TABLE III
SPEED TESTS AT 1500 N AND 23.5 mm OFFSET

Speed (mm/min)	RMSE Force (N)	RMSE Torque (Nm)	Max. Error Force (N)	Max. Error Torque (Nm)
2	22.3	1.0	58.1	1.9
4	21.2	1.2	57.9	1.9
8	18.5	1.4	57.3	2.0
12	16.9	1.5	57.4	2.0
16	16.1	1.5	58.8	2.1
20	14.2	1.6	55.5	2.1

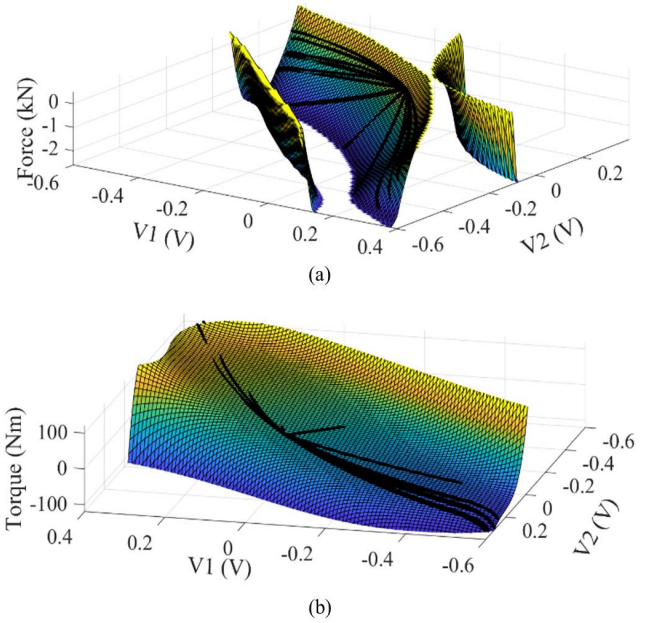


Fig. 12. Data points overlaid with a curve fit for (a) Force and (b) Torque. Saturation shows near ± 120 Nm, causing abrupt change in curvature of the fit.

8.1 N for force and 0.6 Nm for torque, based on a speed change from 2 to 20 mm/min, which corresponds to a loading time of 16 to 1.7 s. For the same speed change, the maximum error changes by 2.6 N and 0.2 Nm for force and torque, respectively.

B. Fitting and Model

The calibration data was used to map the voltage output from the Hall sensors into force and torque signals. Due to the non-linearity of the two-step transduction principle, the voltage sensor outputs cannot be processed using a linear calibration matrix with independent sensitivity coefficients. To address this issue, we used the curve fitting tool in MATLAB (The MathWorks, Inc., Massachusetts, United States) to create two fifth order polynomials to estimate for force and torque independently, as done previously [37], [38]. A fifth order polynomial was chosen as it is the lowest order polynomial which sufficiently fits the output of the sensor in the entire force/torque range covered in the calibration procedure. As can be seen in Fig. 12, the voltages measured by the sensor during the calibration tests were used as inputs to fit the polynomial functions to force and torque data measured by the 6-axis load cell during the same calibration test. The resulting polynomial

TABLE IV
POLYNOMIAL COEFFICIENTS

Coefficient	Force Calibration	Torque Calibration
P00	2.919	0.06982
P10	9312	93.32
P01	1.05×10^4	-152.5
P20	-1.30×10^4	-382.5
P11	-3.62×10^4	-740.4
P02	-1.56×10^4	-339
P30	-1.40×10^5	-1792
P21	-6.15×10^5	-8493
P12	-6.64×10^5	-1.17×10^4
P03	-1.79×10^5	-4681
P40	-6.52×10^5	-4414
P31	-4.04×10^6	-3.92×10^4
P22	-7.10×10^6	-7.84×10^4
P13	-4.76×10^6	-6.51×10^4
P04	-8.83×10^5	-2.18×10^4
P50	-1.00×10^6	-5704
P41	-7.36×10^6	-6.23×10^4
P32	-1.73×10^7	-1.62×10^5
P23	-1.88×10^7	-1.99×10^5
P14	-9.42×10^6	-1.18×10^5
P05	-1.49×10^6	-3.16×10^4

has the form shown in (9), where $v1$ and $v2$ are the voltages output from the Hall sensors. The force and torque coefficients are shown in TABLE IV.

$$F = \sum_{i=0}^5 \sum_{j=0}^{5-i} P_{ij} * v1^i * v2^j \quad (9)$$

The full-scale value of the calibration is 2500 N for force, which is the limit tested by the Instron. The full-scale value for torque is 120 Nm, at which point saturation occurs. The fitting has an R-square value of 0.990 and 0.999 for force and torque, respectively. The RMSE is 65 N and 1.5 Nm for force and torque, respectively, which corresponds to an RMSE of 2.6% and 1.25% of full-scale.

C. Gait Analysis Validation

After calibration, we assessed the performance of our sensor during gait, which, unlike the calibration test, includes forces and torques in non-sensitive directions. Fig. 13 shows the setup for this validation test. The orientation between the SRI sensor and the custom sensor is the same as shown in Fig. 11 (a). The bottom of the two sensors was connected to an off-the-shelf prosthetic foot. The top of the two sensors was attached to a standard 30-mm pylon connecting the foot to a bypass orthosis. Bypass orthoses enable able-bodied individuals to ambulate on prosthetic devices and are commonly used to preliminary validate robotic leg prostheses [39]–[41].

To assess the accuracy of the custom sensor after calibration, an able-bodied subject (male, 24 years old, 174 cm height, 68 kg weight) walked on level ground at a self-selected speed. A total of 56 strides were recorded. Similar to the calibration test, the vertical offset between the 6-axis load cell and the custom sensor was compensated for with (8). The data acquired by the custom sensor and 6-axis load cell was processed offline using MATLAB. Specifically, the least-squares method was used to fit a regression line as shown

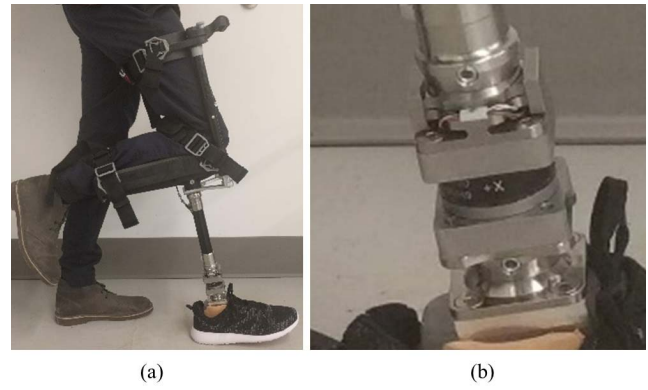


Fig. 13. (a) Experimental setup for validating the sensor on an able-bodied person using a bypass orthosis. (b) Close view of the sensors.

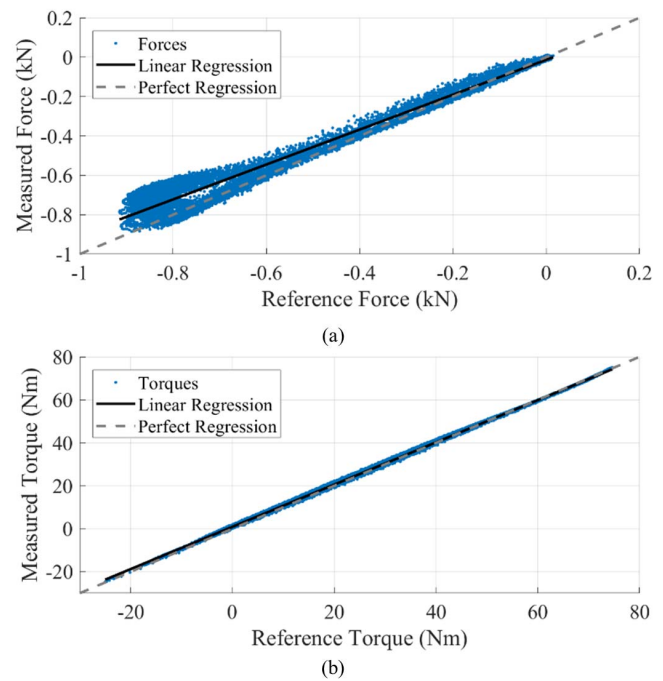


Fig. 14. Linear regression of unfiltered data taken from the prototype sensor and SRI M3713D during walking for (a) Force and (b) Torque.

in Fig. 14. The estimates from the custom sensor had an RMSE of 60 N and 0.86 Nm, nonlinearity of 8.3% and 2.1%, and a Pearson correlation coefficient of 0.993 and 0.999 for force and torque, respectively.

IV. TESTING ON A POWERED PROSTHESIS (CASE USE SCENARIO)

The custom sensor was finally validated in a use-case scenario with the Utah Lightweight Leg, a powered knee and ankle prosthesis [31], [42], [43]. As shown in Fig. 1 (a), the custom sensor was located in between the ankle and knee modules through a standard 30-mm pylon, which is cut to match the specific needs of the users, based on height and residual limb length. The Utah Lightweight Leg uses a finite-state-machine, which requires online estimates of the physical contact with the ground and the shank orientation

with respect to gravity to coordinate the ankle and knee action during ambulation. When the sensor reads a force value along the shank greater than 15% of the body weight, it switches into stance phase, enabling the subject to load their weight on the prosthesis. Conversely, when the sensor reads a ground reaction force lower than 10% of body weight and a shank angle greater than -6 degrees, the finite-state machine switches from stance to swing phase, enabling the subject to take a step. One transfemoral amputee subject (male, 71 years old, 165 cm height, 79 kg weight) was recruited to participate in experiments with the Utah Lightweight Leg. The subject gave written informed consent prior to enrollment. The experimental protocol was approved by the University of Utah Institutional Review Board. The subject completed 100 strides on level ground and 25 strides on stairs ascent and descent. Fig. 15 shows stride data from the amputee subject, normalized by the onset of force detected by the custom sensor. The mean of the strides is shown in black, and the standard deviation is shown in grey. There is a peak of 800 N and 38 Nm in stairs and 1000 N and 70 Nm in walking. For walking, these peaks correspond to 40% and 58% full-scale sensor values in force and torque, respectively. The top row of plots of Fig. 15 show that the sensor can detect heel strike forces with 20 N accuracy. The middle row of plots shows the torque at the ankle. The bottom row of Fig. 15 shows the shank orientation with respect to gravity during walking and stairs. Thus, the sensor was able to provide accurate estimates of the ground reaction force and shank orientation as necessary to control the Utah Lightweight Leg.

V. DISCUSSION

The development of a compact, lightweight force/torque sensor for advanced prosthesis applications is an open challenge. Available solutions mostly consist of retrofitting off-the-shelf load cells to fit within the prosthesis design. This retrofit approach leads to suboptimal design solutions in terms of both weight and size, which are critical factors for prosthesis use. Increasing prosthesis weight leads to higher metabolic effort [12], [13], while the excessive build height may prevent individuals with low clearance from using the prosthesis (e.g., individuals with long residual limbs). The additional weight and height due to the sensor can be minimized by integrating force/torque sensing elements within existing prosthesis components. For example, the Ottobock C-Leg uses an instrumented pylon with embedded force/torque sensing elements [33], which weighs only 40 g more than a standard, non-instrumented pylon, while providing the necessary force/torque sensing to regulate the variable damping in the prosthesis. The C-Leg pylon also has a minimum build height of 90 mm, compared to a minimum of 47 mm for a small pylon. Thus, the C-Leg pylon adds a minimum height of 43 mm. Following a similar approach, we developed the first instrumented male pyramid adapter. The weight of our custom sensor is 150 g, which compares to 84 g for a similar off-the-shelf component. Thus, the force/torque sensing adds only 66 g to the overall prosthesis weight. In addition, our custom sensor has a height of 33.5 mm, compared to about 22 mm for

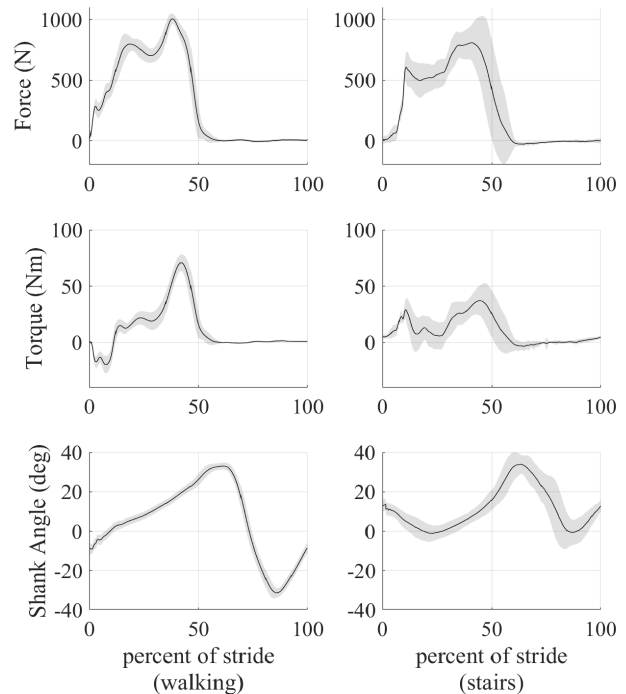


Fig. 15. Data collected with the prototype sensor attached to the top of the ankle of the Utah Lightweight Leg during walking and stairs with an amputee subject. Mean is in black and standard deviation is in grey.

a standard, non-instrumented male pyramid. So, the proposed sensor adds about 1.7 times the weight of the C-Leg sensor but enables a 30 mm smaller height. Thus, our results suggest that instrumenting the pyramid adapter may lead to an increase in weight but lower build height than instrumenting the pylon.

Although comparing research devices can be difficult, as few details are generally provided on the force/torque sensors, there are some important comparisons to be made. The sagittal moment load cell and sensorized foot presented in [44] can sense up to 100 Nm, weighs 120 g, is 35 mm tall, and has a 50x50 mm footprint. Moreover, the sensorized foot weighs 350 g and can measure 1000 N of force. The 3-dimensional force/torque sensor outlined in [18] weighs 360 g, and can sense 1000 N axially and 100 Nm in both the sagittal and the frontal plane. Height and diameter are not specified, but the sensor is larger than 55 mm in diameter and 40 mm in height. In addition, the sensor does integrate a male pyramid on the top, although the bottom is not a standard prosthetic connection. Ottobock has also developed a custom load cell with unknown sensing capabilities which is lighter but has a significantly larger build height than our sensor.

More detailed information can be found on commercial load cells. The lightest and smallest off-the-shelf load cells with sufficient force/torque ranges are the SRI M3713D and the SRI M3564F. The SRI M3713D weighs 110 g, has a diameter of 45 mm, and a height of 19 mm. The SRI M3564F weighs 190 g, has a diameter of 65 mm, and a height of 10 mm. However, integrating these load cells into the prosthesis design requires significant supplemental hardware, ultimately increasing the build height and total weight. For example, the SRI M3713D used in our experiments required

the attachment of stiff plates to operate, which increased the weight of the sensor to 1.1 kg and the height to 43 mm.

Our sensor is smaller and/or lighter than most other research devices. However, there are design tradeoffs made in order to achieve this result. The most notable tradeoff is that our sensor can only measure axial force and sagittal moment. This design choice is motivated by the fact that axial force and sagittal moment are commonly used for the control of advanced prostheses [9]. Thus, designing a sensor that only measures these two degrees of freedom may not significantly limit use of the custom sensor in advanced prostheses. The SRI M3713D (Sunrise Instruments) has crosstalk of 2% full-scale (6400 N, 112 Nm), non-linearity of 0.5% full-scale, and hysteresis of 0.5% full-scale. Our experimental results show that the RMSE of our custom sensor were 60 N and 0.86 Nm, and the nonlinearity was 8.3% and 2.1% for force and torque, respectively, as shown in Section III.C. With the sensitivity to this relatively small torque value, the sensor has the potential for real-time powered prosthesis control. During our amputee testing, the sensor was set to trigger the controller finite-state machine when the axial force exceeded 15% of body weight. However, no closed-loop torque control was attempted.

A possible limitation of the proposed experimental approach is that the calibration was performed in compression only, as compressive loads are the only loads created in the gait cycle, except for small tension loads due to the weight and inertia of the prosthetic foot. A further limitation is that the calibration did not cover the entire span of voltages that could be output by the sensor, so the sensor may provide inaccurate readings for certain force and torque combinations that were not tested. For example, a pure torque was not applied during calibration, so the resulting polynomial fit may not be accurate if a pure torque is applied. However, the validation experiments with able-bodied and amputee subject suggest that this drawback did not affect the effectiveness of the proposed sensor, most likely as the sensor never experiences pure torque during its normal use.

The sensor has the potential to be developed at a lower cost compared to traditional strain-gauge force/torque load cells. The cost of the mechanical and electrical components was ~\$1500, which may be reduced by scaling the production. Notably, our custom sensor does not require highly precise placement of strain gauges on the mechanical structure, which can be a significant production cost for strain-gauge load cells. The magnets and Hall sensors can more easily tolerate misalignment, do not require a controlled environment to be placed on the sensor, and do not require analog signal amplification. Commercial force/torque load cells which handle 112 Nm, such as the SRI M3713D, can be bought for \$3,200 without data acquisition electronics. The only force/torque sensor available on the market specifically for prosthetics use is the iPecs™, which costs \$16,900. The iPecs™ can provide 6-axis force torque reading but has a height of over 20 mm, weighs 280 g, and requires additional hardware to attach to a prosthesis. Thus, the iPecs is not ideal for use in advanced prostheses.

Future work will focus on exploring applications of the sensor for gait analysis with individuals using off-the-shelf

prostheses. Instrumented treadmills or walkways are commonly used in combination with motion capture to perform gait analysis. However, the required instrumentation is expensive and limited to use in a laboratory setting. An alternative solution consists of using load cells in line with the prosthesis together with inertial measurement. This alternative approach provides greater flexibility and lower cost although it has lower accuracy. In addition, future work will focus on using the sensor for closed-loop control of torque in powered prosthesis such as the Utah Lightweight Knee and Polycentric Ankle.

VI. CONCLUSION

In this paper we present a novel force/torque sensor for advanced prosthetics applications. The custom sensor is based on large deformations in a cantilever beam design, which are measured through magnetic field sensing. The force/torque sensing elements are embedded in the structure of a pyramid adapter to minimize the overall size and weight, maximizing usability. The extended bench-top characterization shows that the sensor error, linearity, and hysteresis are appropriate for prosthesis use. In addition, the sensor was preliminarily validated in a case use scenario with an above-knee amputee using a powered ankle and knee prosthesis. Results show that the proposed instrumented pyramid adapter fits within size and weight requirements and has the sensitivity and resolution needed for use with powered prostheses.

ACKNOWLEDGMENT

The authors would like to thank Jeff Kessler and Alik Nielsen for their knowledge and assistance in calibrating the sensor. The authors would also like to thank Minh Tran, Sarah Hood, and Marshall Ishmael for their help throughout the project.

REFERENCES

- [1] K. Ziegler-Graham, E. J. MacKenzie, P. L. Ephraim, T. G. Trivison, and R. Brookmeyer, "Estimating the prevalence of limb loss in the United States: 2005 to 2050," *Arch. Phys. Med. Rehabil.*, vol. 89, no. 3, pp. 422–429, 2008.
- [2] R. Sinha, W. J. van den Heuvel, and P. Arokiasamy, "Factors affecting quality of life in lower limb amputees," *Prosthet. Orthot. Int.*, vol. 35, no. 1, pp. 90–96, Mar. 2011.
- [3] R. L. Waters and S. Mulroy, "The energy expenditure of normal and pathologic gait," *Gait Posture*, vol. 9, no. 3, pp. 207–231, Jul. 1999.
- [4] C. J. C. Lamoth, E. Ainsworth, W. Polonski, and H. Houdijk, "Variability and stability analysis of walking of transfemoral amputees," *Med. Eng. Phys.*, vol. 32, no. 9, pp. 1009–1014, Nov. 2010.
- [5] C. Kendell, E. D. Lemaire, N. L. Dudek, and J. Kofman, "Indicators of dynamic stability in transtibial prosthesis users," *Gait Posture*, vol. 31, no. 3, pp. 375–379, Mar. 2010.
- [6] J. M. Stepien, S. Cavenett, L. Taylor, and M. Crotty, "Activity levels among lower-limb amputees: Self-report versus step activity monitor," *Arch. Phys. Med. Rehabil.*, vol. 88, no. 7, pp. 896–900, Jul. 2007.
- [7] D. R. Bassett, Jr., H. R. Wyatt, H. Thompson, J. C. Peters, and J. O. Hill, "Pedometer-measured physical activity and health behaviors in United States adults," *Med. Sci. Sports Exerc.*, vol. 42, no. 10, pp. 1819–1825, Oct. 2010.
- [8] M. Goldfarb, "Consideration of powered prosthetic components as they relate to microprocessor knee systems," *JPO J. Prosthetics Orthot.*, vol. 25, pp. P65–P75, Oct. 2013.
- [9] M. Goldfarb, B. E. Lawson, and A. H. Shultz, "Realizing the promise of robotic leg prostheses," *Sci. Transl. Med.*, vol. 5, no. 210, pp. 210–215, Nov. 2013.

- [10] D. A. Winter, *Biomechanics and Motor Control of Human Movement*, 2nd ed. Hoboken, NJ, USA: Wiley, 1990.
- [11] A. R. Tilley, *The Measure of Man and Woman*. New York, NY, USA: Watson-Guptill, 1993.
- [12] J. D. Smith and P. E. Martin, "Effects of prosthetic mass distribution on metabolic costs and walking symmetry," *J. Appl. Biomech.*, vol. 29, no. 3, pp. 317–328, Jun. 2013.
- [13] S. Mattes, P. E. Martin, and T. D. Royer, "Walking symmetry and energy cost in persons with unilateral transtibial amputations: Matching prosthetic and intact limb inertial properties," *Arch. Phys. Med. Rehabil.*, vol. 81, pp. 561–568, May 2000.
- [14] T. Elery, S. Rezazadeh, C. Nesler, J. Doan, H. Zhu, and R. D. Gregg, "Design and benchtop validation of a powered knee-ankle prosthesis with high-torque, low-impedance actuators," in *Proc. IEEE Int. Conf. Robot. Automat. (ICRA)*, May 2018, pp. 2788–2795.
- [15] H. Huang, F. Zhang, L. J. Hargrove, Z. Dou, D. R. Rogers, and K. B. Englehart, "Continuous locomotion-mode identification for prosthetic legs based on neuromuscular-mechanical fusion," *IEEE Trans. Biomed. Eng.*, vol. 58, no. 10, pp. 2867–2875, Oct. 2011.
- [16] T. Lenzi, M. Cempini, J. Newkirk, L. J. Hargrove, and T. A. Kuiken, "A lightweight robotic ankle prosthesis with non-backdrivable cam-based transmission," in *Proc. Int. Conf. Rehabil. Robot. (ICORR)*, Jul. 2017, pp. 1142–1147.
- [17] F. C. Sup and M. Goldfarb, "Design of a pneumatically actuated transfemoral prosthesis," in *Proc. ASME Int. Mech. Eng. Congr. Expo.*, Jan. 2006, pp. 1419–1428.
- [18] F. Sup, A. Bohara, and M. Goldfarb, "Design and control of a powered transfemoral prosthesis," *Int. J. Robot. Res.*, vol. 27, no. 2, pp. 263–273, 2008.
- [19] B. E. Lawson, J. Mitchell, D. Truex, A. Shultz, E. Ledoux, and M. Goldfarb, "A robotic leg prosthesis: Design, control, and implementation," *IEEE Robot. Automat. Mag.*, vol. 21, no. 4, pp. 70–81, Dec. 2014.
- [20] A. K. LaPré, B. R. Umberger, and F. C. Sup, "A robotic ankle-foot prosthesis with active alignment," *ASME J. Med. Devices*, vol. 10, no. 2, 2016, Art. no. 025001.
- [21] T. Lenzi, J. Sensinger, J. Lipsey, L. Hargrove, and T. Kuiken, "Design and preliminary testing of the RIC hybrid knee prosthesis," in *Proc. Annu. Int. Conf. IEEE Eng. Med. Biol. Soc.*, Aug. 2015, pp. 1683–1686.
- [22] P. Cherelle, V. Grosu, A. Matthys, B. Vanderborght, and D. Lefeber, "Design and validation of the ankle mimicking prosthetic (AMP-) foot 2.0," *IEEE Trans. Neural Syst. Rehabil. Eng.*, vol. 22, no. 1, pp. 138–148, Jan. 2014.
- [23] S. Pandit, A. K. Godiyal, A. K. Vimal, U. Singh, D. Joshi, and D. Kalyanasundaram, "An affordable insole-sensor-based trans-femoral prosthesis for normal gait," *Sensors*, vol. 18, no. 3, p. 706, 2018.
- [24] E. J. Rouse, L. M. Mooney, and H. M. Herr, "Clutchable series-elastic actuator: Implications for prosthetic knee design," *Int. J. Robot. Res.*, vol. 33, no. 13, pp. 1611–1625, 2014.
- [25] H. Choi, K. Seo, S. Hyung, Y. Shim, and S. C. Lim, "Compact Hip-Force sensor for a gait-assistance exoskeleton system," *Sensors*, vol. 18, p. 566, Feb. 2018.
- [26] Q. Nie and F. C. Sup, "A soft four degree-of-freedom load cell based on the Hall effect," *IEEE Sensors J.*, vol. 17, pp. 7355–7363, Nov. 2017.
- [27] M. Grimmer *et al.*, "A powered prosthetic ankle joint for walking and running," *Biomed. Eng. Online*, vol. 15, no. 13, p. 141, 2016.
- [28] A. Pagel, R. Ranzani, R. Riener, and H. Vallery, "Bio-inspired adaptive control for active knee exoprosthetics," *IEEE Trans. Neural Syst. Rehabil. Eng.*, vol. 25, no. 12, pp. 2355–2364, Dec. 2017.
- [29] D. A. Winter and S. E. Sienko, "Biomechanics of below-knee amputee gait," *J. Biomech.*, vol. 21, no. 5, pp. 361–367, 1988.
- [30] S. R. Koehler, Y. Y. Dhaher, and A. H. Hansen, "Cross-validation of a portable, six-degree-of-freedom load cell for use in lower-limb prosthetics research," *J. Biomech.*, vol. 47, no. 6, pp. 1542–1547, Apr. 2014.
- [31] M. Tran, L. Gabert, M. Cempini, and T. Lenzi, "A lightweight, efficient fully powered knee prosthesis with actively variable transmission," *IEEE Robot. Automat. Lett.*, vol. 4, no. 2, pp. 1189–1193, Apr. 2019.
- [32] J. F. Lehmann, R. Price, R. Okumura, K. Questad, B. J. De Lateur, and A. Négretot, "Mass and mass distribution of below-knee prostheses: Effect on gait efficacy and self-selected walking speed," *Arch. Phys. Med. Rehabil.*, vol. 79, no. 2, pp. 162–168, Feb. 1998.
- [33] L. J. Marks and J. W. Michael, "Science, medicine, and the future: Artificial limbs," *Proc. BMJ*, vol. 323, no. 7315, pp. 732–735, Sep. 2001.
- [34] W. C. Young and R. G. Budynas, *Roark's Formulas for Stress and Strain*, 7th ed. New York, NY, USA: McGraw-Hill, 2011.
- [35] *Hall Effect Sensing and Application*. 2011.
- [36] D. A. Winter, "Kinematic and kinetic patterns in human gait: Variability and compensating effects," *Hum. Mov. Sci.*, vol. 3, nos. 1–2, pp. 51–76, Mar./Jun. 1984.
- [37] S. M. M. De Rossi *et al.*, "Sensing pressure distribution on a lower-limb exoskeleton physical human-machine interface," *Sensors*, vol. 11, no. 1, pp. 207–227, Dec. 2010.
- [38] T. Lenzi *et al.*, "Measuring human-robot interaction on wearable robots: A distributed approach," *Mechatronics*, vol. 21, no. 6, pp. 1123–1131, Sep. 2011.
- [39] T. Lenzi, L. Hargrove, and J. W. Sensinger, "Preliminary evaluation of a new control approach to achieve speed adaptation in robotic transfemoral prostheses," in *Proc. IEEE/RSJ Int. Conf. Intell. Robots Syst.*, Sep. 2014, pp. 2049–2054.
- [40] T. Lenzi, L. J. Hargrove, and J. W. Sensinger, "Minimum jerk swing control allows variable cadence in powered transfemoral prostheses," in *Proc. 36th Annu. Int. Conf. IEEE Eng. Med. Biol. Soc.*, Aug. 2014, pp. 2492–2495.
- [41] T. Lenzi, M. Cempini, L. J. Hargrove, and T. A. Kuiken, "Actively variable transmission for robotic knee prostheses," in *Proc. IEEE Int. Conf. Robot. Automat. (ICRA)*, May 2017, pp. 6665–6671.
- [42] M. Cempini, L. J. Hargrove, and T. Lenzi, "Design, development, and bench-top testing of a powered polycentric ankle prosthesis," in *Proc. IEEE/RSJ Int. Conf. Intell. Robots Syst.*, Sep. 2017, pp. 1064–1069.
- [43] S. A. Hood and T. Lenzi, "Preliminary analysis of positive knee energy injection in a transfemoral amputee walking with a powered prosthesis," in *Proc. Annu. Int. Conf. IEEE Eng. Med. Biol. Soc. (EMBC)*, Jul. 2018, pp. 1821–1824.
- [44] F. Sup, H. A. Varol, J. Mitchell, T. Withrow, and M. Goldfarb, "Design and control of an active electrical knee and ankle prosthesis," in *Proc. 2nd IEEE RAS EMBS Int. Conf. Biomed. Robot. Biomechatronics*, Oct. 2008, pp. 523–528.



Lukas Gabert received the B.Sc. degree in mechanical engineering from the New Mexico Institute of Mining and Technology, Socorro, NM, USA, in 2016, and the M.Sc. degree in mechanical engineering from the University of Utah, Salt Lake City, UT, USA, in 2019. He is currently pursuing the Ph.D. degree in mechanical engineering with the University of Utah.

His research interests include sensing methods and control algorithms for lower limb prostheses.



Tommaso Lenzi (S'11–M'13) received the M.Sc. degree in biomedical engineering from the University of Pisa, Pisa, Italy, in 2008, and the Ph.D. degree in biorobotics from Scuola Superiore Sant'Anna, Pisa, in 2012.

He is currently an Assistant Professor with the Department of Mechanical Engineering, University of Utah. He is also core faculty with the Utah Robotics Center. His main research interests include robotics, mechatronics, and rehabilitation medicine.